Available online at www.sciencedirect.com

ScienceDirect

Underground Space 25 (2025) 19–32

www.keaipublishing.com/undsp

Research Paper

Laboratory test on three-dimensional stress state of the surrounding soil during tunnel excavation

Yu Tian [a,*], Hao Chen [a], Junquan Wen [b], Abdul Motalleb Qaytmas [a], Dechun Lu [a], Xiuli Du [a]

[a] *Institute of Geotechnical and Underground Engineering, Beijing University of Technology, Beijing 100124, China*
[b] *Guangzhou Highway Engineering Group Co., Ltd., Guangzhou 510075, China*

Received 12 November 2024; received in revised form 23 April 2025; accepted 13 May 2025
Available online 10 September 2025

Abstract

During tunnel excavation, the surrounding soil experiences complex stress redistribution, which is the root cause of the ground deformation and other engineering disasters. Many researchers have studied this issue through numerical simulations, but the results depend on the soil constitutive model and simulation strategy for the excavation process. In this paper, a large-scale laboratory test is conducted using a scaled shield machine, and the three-dimensional stress state of the surrounding soil is measured by a special earth pressure cell. Test data shows that the normal stress components and principal stresses above the crown decrease, and the stress path on the normalized deviatoric plane reaches the failure envelope determined by Matsuoka–Nakai criterion. Due to the misalignment between the stress release direction and principal directions of the geostatic stresses, shear stress is generated in the physical space, which explains the principal stress rotation of the surrounding soil near the shoulder. Near the sidewall, the major principal stress σ_1 is vertical and remains basically unchanged, the intermediate principal stress σ_2 is along the longitudinal direction and increases when the cutterhead reaches the monitoring section, while the minor principal stress σ_3 is along the transversal direction and decreases. On the deviatoric plane, stress paths near the foot and invert have similar development tendencies as those near the shoulder and crown, respectively. Therefore, the influence of the complex stress state on soil behaviours should be considered to provide a reasonable analysis for the tunnel excavation problem.

Keywords: Tunneling; Three-dimensional stress state; Surrounding soil; Laboratory test; Principal stress rotation

1 Introduction

Tunnel excavation leads to the stress redistribution of the surrounding soil, which is the root cause of the ground deformation. Excessive ground deformation will profoundly influence the safety of the tunnel engineering and adjacent structures (X. Li et al., 2016; Ahmed et al., 2023; Ng et al., 2024; Li et al., 2025). Therefore, a comprehensive recognition of the stress state of the surrounding soil is critical for the tunnel design, construction safety management, and subsequent maintenance. Researchers have utilized various methods to study the stress state of the surrounding soil during tunnel excavation. Analytical solution methods can compute the stress release around the tunnel (Massinas & Sakellariou, 2009; Wang et al., 2020), but they must rely on simplified assumptions and idealized boundary conditions to accomplish the solution. Numerical simulations, including finite element method (FEM) and discrete element method (DEM), are widely used to simulate the stress redistribution of the surrounding soil under complex conditions (Zheng et al., 2015; Huang et al., 2023). The simulation results provide detailed insights into understanding the influence of tunnel excavation on the environment.

At first, Lee and Rowe (1989) conducted a two-dimensional (2D) FEM simulation to determine the

* Corresponding author.
E-mail address: tianyu@bjut.edu.cn (Y. Tian).
Peer review under the responsibility of Tongji University

https://doi.org/10.1016/j.undsp.2025.05.003

effective stress path of the surrounding soil during tunnel excavation. They observed significant rotation of the principal stress axes near the tunnel shoulder. Wang et al. (2012) simulated the excavation of a shallow-buried tunnel in clay strata and found that the radial stress at the crown and sidewall increased after lining was installed. However, the tangential stress at the crown decreased, while that at the sidewall increased slightly. Based on the tunnel excavation simulation in gravel, Zhang et al. (2021a) identified the boundary of the excavation disturbed zone using the displacement mutation points of the monitored path. Through 2D DEM simulation, Jiang and Yin (2012) analyzed the variation of the earth pressure acting on the lining with the ground volume loss increasing, and examined the stress path of the surrounding soil. They found that at the positions above the tunnel, the normal stress slightly decreased, while the decrease in the shear stress was considerable. Near the sidewall, however, the normal stress slightly increased due to the soil arching effect. Along these stress paths, soil (Barla, 2008; Jiang et al., 2017) and rock (Feng et al., 2020) exhibited special deformation behaviours compared with the stress–strain relationship under conventional loading conditions. Especially for the stress path near the sidewall, geomaterials had the greatest deformation, so the sidewall should be a focal point during tunnel excavation.

The above work focused on the stress state of the surrounding soil on the tunnel transversal or longitudinal plane. However, tunnel engineering often involves complex spatial structures, while 2D analysis may overlook the stress variation and deformation of the surrounding soil, leading to potential inaccuracies and risks (Mašín, 2009). Three-dimensional (3D) numerical simulation can provide a more reasonable solution for this issue. Eberhardt (2001) investigated the principal stress magnitudes and directions at the crown and sidewall under four different initial stress states. They also revealed that the simulation results were related to the constitutive model adopted for the surrounding rock. Y. Li et al. (2016) simulated the tunnel intersection using 3D FEM and found a stress concentration near the sidewall. The stress state at the tunnel intersection reached the plastic zone earlier than that in the other areas. Vinoth and Aswathy (2023) compared the extent of the loosened region and soil arching region in silty and sandy soils. The variation amplitude of three normal stresses in silty soil was predominantly larger than that in sandy soil. Gu et al. (2023) simulated the rock fracture induced by deep tunnel excavation, and observed a gradual decrease in the maximum deviatoric stress from the high-risk to low-risk fracture zones. The 3D FEM simulation of Lin et al. (2019) showed that when the burial depth of the monitoring point was shallow, the longitudinal normal stress gradually decreased, the transversal normal stress increased, while the vertical normal stress remained constant during tunneling. However, when the monitoring point was close to the crown, the vertical normal stress decreased rapidly as the tunnel face arrived. Fang et al. (2022) and Yuan et al. (2024) introduced a 3D constitutive model considering the soil anisotropy and non-coaxiality into the FEM simulation, and acquired excellent predictions for the ground surface settlement and lining longitudinal stress. On the other hand, DEM was used by Lyu et al. (2020) to determine the principal stress directions of the surrounding soil in 3D space as the cutterhead advanced. The advantage of DEM is that it can locate the soil arching intuitively by displaying the force chains between particles.

In addition to the aforementioned studies, some researchers conducted physical model tests to measure the stress state of the surrounding soil during tunnel excavation. Berthoz et al. (2018) performed a series of scaled model tests and used the embedded sensors to measure the ground stress and subsidence induced by tunneling. Based on the measured results, they determined the extent of the influence zone and soil arching. Li et al. (2024) manufactured a small earth pressure balance shield machine, and carried out a tunnel excavation model test in a large soil box. With the shield machine advancing, the vertical earth pressure above the crown was found to decrease while the horizontal earth pressure near the sidewall increased. The variation amplitude of these stresses gradually shrank as the cutterhead got away from the monitoring points. Tian et al. (2023) adopted a special 3D earth pressure cell to measure all six stress components (including three normal stress components and three shear stress components) of the surrounding soil. They drew the stress paths on the meridian plane, and analyzed the magnitudes and directions of the major and minor principal stresses. However, information about the intermediate principal stress and the stress state variation in 3D space was not provided.

Because mechanical behaviours of soil are significantly influenced by the intermediate principal stress, it is necessary to do 3D analysis to obtain accurate results, especially for complex geotechnical problems like tunnel excavation. However, due to the limitations of experimental apparatus and sensors, the 3D stress state of the surrounding soil is usually investigated by numerical simulations, rather than in-situ or laboratory monitoring. This paper addresses the gap by conducting a large-scale model test in which the tunneling-induced ground stresses along different directions are measured. Relative values between three principal stresses near the tunnel crown, shoulder, sidewall, foot, and invert are illustrated in 3D space. Based on the measured direction angles of the principal stresses, the phenomenon of principal stress rotation during tunnel excavation is analyzed.

2 Tunnel excavation model test

A large-scale model test is conducted to simulate the shield tunnel excavation process in the laboratory. What follows introduces the apparatus and sensors used in this test.

2.1 Shield machine

The total length of the shield machine is more than 2300 mm, as shown in Fig. 1(a). Two leading screws, which are driven by motor I, can rotate and force the lining to move forward at a given speed. Another two rods without thread are added to limit the deviation of the shield advancing direction. The lining is made of a complete polyethylene tube, with a diameter of 280 mm and a length of 2000 mm. In front of the lining, there is a cutterhead whose rotation is controlled by motor II. Soil in the model box is excavated as the cutterhead rotates, and then discharged by a screw conveyor from the end of the lining. Many pressure sensors are installed on the cutterhead and in the soil chamber (see Fig. 1(b)), so that the earth pressure balance can be realized by adjusting the advancing speed of the cutterhead (through motor I) and the rotation speed of the screw conveyor (through motor III). Parameters about the running state of the shield machine, including the torque of the cutterhead and screw conveyor, as well as the jacking force of the leading screws, are monitored in real time. The size of the model box is 2000 mm × 2000 mm × 1500 mm (length × width × height). The cutterhead enters the model box via a hole, followed by the lining, as a simulation of the shield excavation and support.

2.2 Sand

The model box is filled with silica sand. The diameter of the sand particles ranges between 1 and 3 mm, so that the gradation is poor. The particle itself is extremely hard and angular, with a specific gravity of 2.65. The sand is dry to eliminate the effects of pore water pressure and capillary suction. According to the standard methods, the maximum and minimum void ratios are 0.987 and 0.535, respectively. In the tunnel excavation model test, the relative density is set to be 80%, which corresponds to a void ratio of 0.625. A series of direct shear tests is conducted to measure the shear stress-displacement relation curves of the sand samples (see Fig. 2(a)). The normal stresses (σ_n) are 50, 100, and 200 kPa, respectively. Based on the peak strengths, the internal friction angle φ is determined to be 21.9° (see Fig. 2(b)). During the filling process, the sand density is strictly controlled by compacting the ground layer by layer. Finally, the ground height reaches 1340 mm.

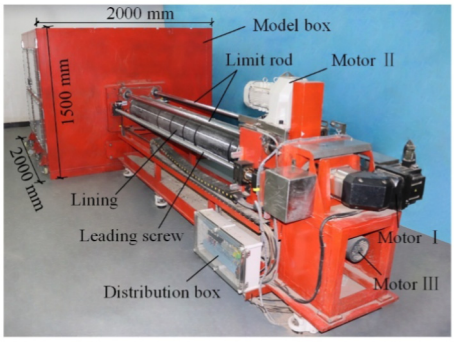

(a)

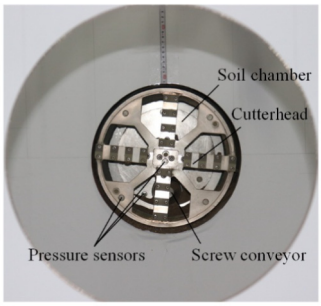

(b)

Fig. 1. Shield machine in the tunnel excavation model test. (a) Back view, and (b) front view.

2.3 Data monitoring

2.3.1 3D earth pressure cell

The stress state of the surrounding soil is measured by a special 3D earth pressure cell. The shape of the 3D earth pressure cell is approximately spherical. It consists of seven conventional earth pressure sensors that are oriented

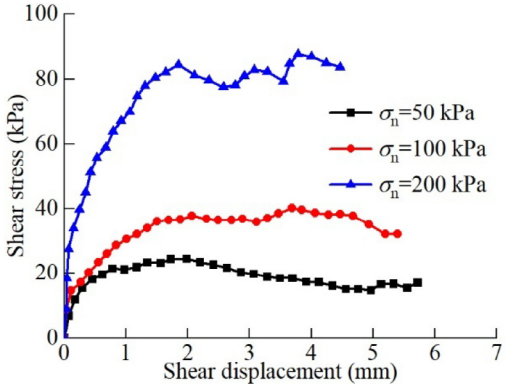

(a)

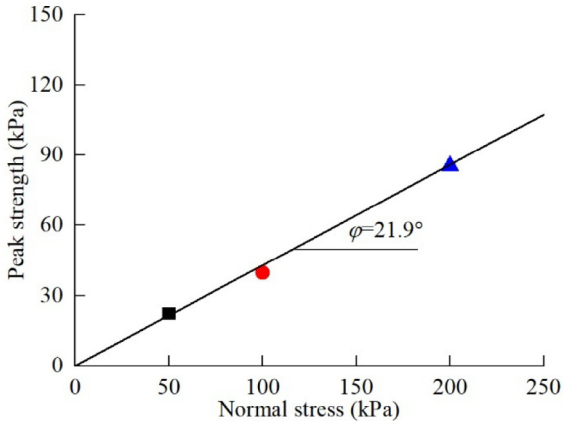

(b)

Fig. 2. Determination of the sand strength using direct shear tests. (a) Shear stress-displacement relation curves, and (b) best-fitted failure line.

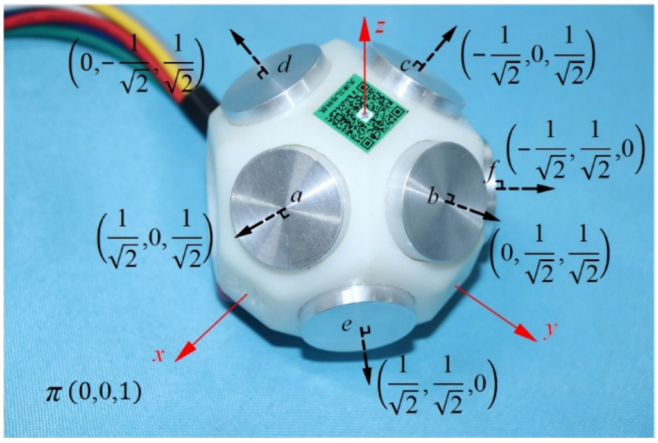

Fig. 3. Structure of the 3D earth pressure cell.

towards different directions. Figure 3 shows six sensors and their unit outer normal vectors, while the last one is installed at the bottom with its unit outer normal vector being (0, 0, 1). Each earth pressure sensor can measure the normal stress along the corresponding direction. According to the equilibrium condition, the normal stress acting on sensor a, i.e., $\sigma_{n,a}$, can be calculated by

$$\sigma_{n,a} = \sigma_x l_a^2 + \sigma_y m_a^2 + \sigma_z n_a^2 + 2\tau_{xy} l_a m_a + 2\tau_{yz} m_a n_a + 2\tau_{zx} n_a l_a, \quad (1)$$

where (l_a, m_a, n_a) is the unit outer normal vector of sensor a; σ_x, σ_y, σ_z, τ_{xy}, τ_{yz}, and τ_{zx} represent the 3D stress state of the surrounding soil in the physical space (x, y, z), σ_x is the transversal normal stress, σ_y is the longitudinal normal stress, σ_z is the vertical normal stress, τ_{xy} is the shear stress in the horizontal plane, τ_{yz} is the shear stress in the longitudinal plane, and τ_{zx} is the shear stress in the transversal plane. Here, x- and y-axes constitute the horizontal plane, and are perpendicular and parallel to the shield advancing direction, respectively; while z-axis is vertically downward. If we measure six normal stresses along different directions, σ_x, σ_y, σ_z, τ_{xy}, τ_{yz}, and τ_{zx} can be worked out by combining six equations like Eq. (1). The seventh earth pressure sensor helps to improve the measurement precision and reliability. In this test, we first calculate seven sets of σ_x, σ_y, σ_z, τ_{xy}, τ_{yz}, and τ_{zx} by randomly selecting the measured results of six earth pressure sensors, and then obtain their average values as the 3D stress state of the surrounding soil. Note that the radius of the 3D earth pressure cell is about 33 mm, so that strictly speaking, the measured result is the average stress within a certain range, rather than the stress state of a point.

2.3.2 Monitoring points

According to many FEM simulation results (Wang et al., 2023; Zhang et al., 2021b), stress states near the tunnel crown, shoulder, sidewall, foot, and invert are very representative, where soil failure or rock fracture appears first during tunnel excavation. Therefore, five 3D earth pressure cells are buried at these points around the tunnel. Their coordinates in the physical space are displayed in Fig. 4. Except for the 3D earth pressure cell below the invert, the distance from the monitoring points to the tunnel center is 280 mm, which is equal to the tunnel diameter. Besides, the 3D earth pressure cell above the crown is buried on the tunnel transversal plane that corresponds to a shield advancing distance of 700 mm, i.e., y = 700 mm; while the other four monitoring points are located at y = 600 mm.

When the 3D earth pressure cell is buried, not only must its position conform to the above scheme, but also its attitude should be regulated to ensure that the coordinate axes of itself (see Fig. 3) are consistent with the physical coordinate axes (see Fig. 4). The following measures are taken to meet these requirements. Before the model box is filled, some rulers are pasted on the inner walls. Based on the graduation, ropes can be arranged along the x-axis and y-axis of the physical space to determine the horizontal position and direction of the 3D earth pressure cell. The burial depth, i.e., z-coordinate, of the cell is fixed by virtue of a horizontal infrared ray. After that, we lay a bubble level on the top surface of the 3D earth pressure cell, and regulate the cell's attitude to keep the bubble in the middle of the bubble level. Then, the bubble level is rotated by 90°, and the cell's attitude is regulated once again. These procedures are repeated many times until the bubble is always centered, no matter which direction the bubble level is laid, so that the z-axis of the 3D earth pressure cell is physically vertical.

2.4 Excavation process

The burial depth of the crown is 560 mm (see Fig. 4), so that the cover-to-diameter ratio of the tunnel is two. The advancing speed of the cutterhead is set to be 5 mm/min. Note that when the shield machine is designed, the geometric similarity ratio is 1:45, while the time similarity ratio is taken to be $1{:}\sqrt{45}$ in this test. So, the corresponding actual value of the advancing speed of the cutterhead is 33.5 mm/min, which conforms to the reality of shield excavation. Besides, the rotation speed of the cutterhead

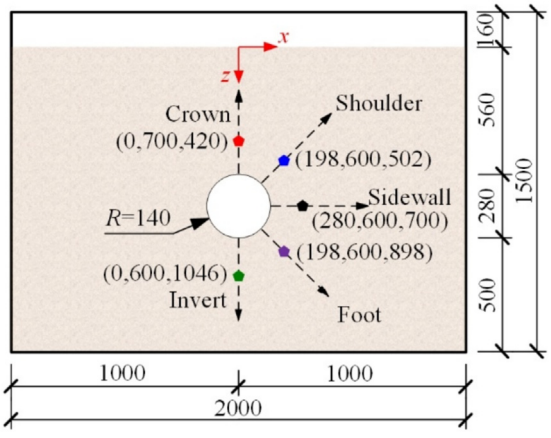

Fig. 4. Coordinates of the monitoring points. (Unit: mm)

is 1 r/min, and that of the screw conveyor is 6 r/min. Using the above construction parameters, the excavation face can be kept stable, and the stress state variation can be captured by the 3D earth pressure cell sensitively.

It is necessary to note that the laboratory test in this work belongs to a constant gravity model test, which cannot reproduce the stress state of soil in practical engineering. Because soil is a kind of frictional material, its mechanical behaviours are significantly dependent on the confining pressure. The stress–strain relation of soil is also nonlinear, with different strength or stiffness under different confining pressures, even if these indexes are normalized. In the model box, the maximum vertical geostatic stress is only 21.4 kPa. Under such a low confining pressure, soil undergoes obvious dilation, which offsets the tunneling-induced volume loss to some degree and prevents the volume loss from spreading far. Therefore, this test does not intend to simulate any practical engineering, and the measured results can only reflect the stress redistribution pattern under the specific experimental conditions.

3 Measured results about stress components

This section introduces the original data about six stress components in the physical space, i.e., σ_x, σ_y, σ_z, τ_{xy}, τ_{yz}, and τ_{zx}. Their initial values are assumed to be equal to the geostatic stresses at the monitoring point. The coefficient of earth pressure at rest K_0 is calculated by 1–sin φ. To avoid the influence of this theoretical formula, our introduction will mainly focus on the variation of the stress components, rather than their absolute values, in the process of tunnel excavation.

3.1 Tunnel crown

Figure 5 shows the stress components measured by the 3D earth pressure cell above the crown. The horizontal coordinate axis is the distance from the cutterhead to the monitoring section normalized by the tunnel diameter D. It can be seen that the transversal normal stress σ_x and vertical normal stress σ_z decrease rapidly when the cutterhead is just beneath the 3D earth pressure cell, which means a loosened region is caused by tunnel excavation. But because neither σ_x nor σ_z reduces to zero, the surrounding soil does not collapse completely. After the cutterhead passes through the monitoring section by 0.2D, the stress components remain basically unchanged so that tunnel excavation has no impact on the monitoring point any longer. In the laboratory test of Li et al. (2024), where conventional earth pressure sensors were used to measure the normal stress variation, σ_z was also found to decrease when the cutterhead reached the monitoring section and stabilize when the cutterhead passed by 0.2D. Compared with σ_x and σ_z, the decrease of the longitudinal normal stress σ_y appears much earlier. This implies that the stress release along the longitudinal direction can propagate faster than that along the transversal direction. In theory, σ_y is generated by the support pressure applied by the cutterhead to the tunnel face. Due to the over-excavation in this test, the insufficient support pressure with respect to the horizontal geostatic stress leads to the decrease of σ_y. However, as the cutterhead moves away, σ_y will recover its initial value. These measured results are consistent with the FEM simulations of Lin et al. (2019). Among all three shear stresses, the variation amplitude of τ_{zx} is particularly limited, indicating that the principal stress directions on the transversal plane (i.e., x-z plane) hardly rotate. For the surrounding soil above the crown, principal stress rotation mainly occurs on the longitudinal plane (i.e., y-z plane) and horizontal plane (i.e., x-y plane). This phenomenon will be analyzed deeply in Section 5.

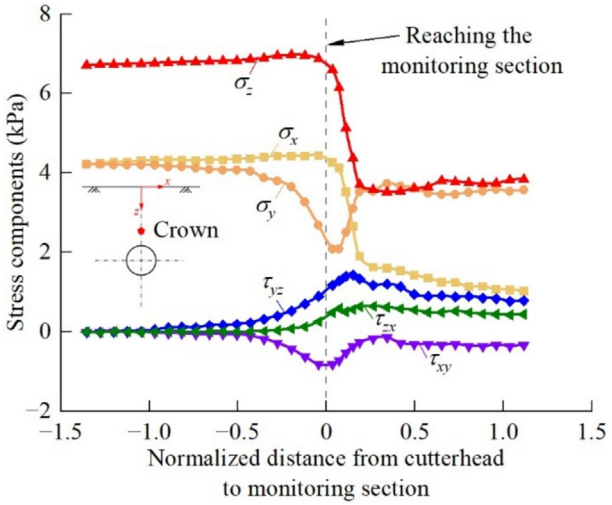

Fig. 5. Stress components of the surrounding soil above the crown.

3.2 Tunnel shoulder

Figure 6 shows the stress components near the shoulder. Observe that σ_x and σ_z have the similar variation rule, just like those above the crown. The difference lies in the fact that the variation amplitude of σ_x and σ_z near the shoulder is much smaller, and they increase slightly before the cutterhead reaches the monitoring section. Besides, σ_y also first increases and then decreases, which is contrary to the crown. We can deduce that the loosened region is mainly concentrated above the crown, while the degree of normal stress release near the shoulder is at a low level. Instead, the advancement of the shield machine squeezes the surrounding soil here, leading to the initial increase in the normal stresses. Similar phenomena and conclusions are obtained by Li et al. (2024). At the end of the excavation process, the values of σ_x, σ_y, and σ_z get back to the geostatic stresses. What deserves special concern is the variation of shear stresses. As the shear stress on the transversal plane, τ_{zx} increases dramatically once the cutterhead reaches the monitoring section. Its variation amplitude is the largest among all six stress components. In theory, τ_{zx} is generated by the misalignment between the stress

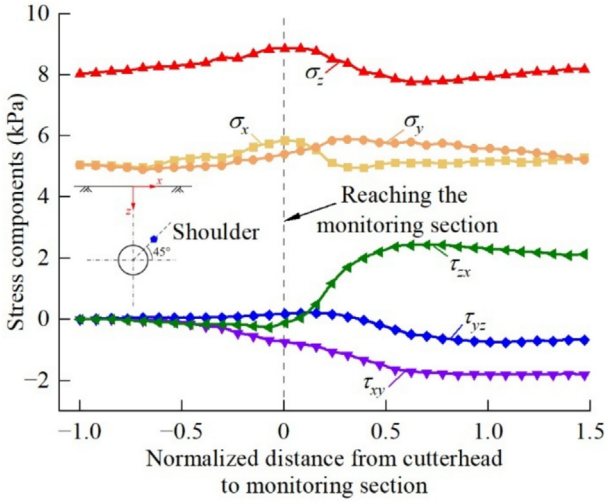

Fig. 6. Stress components of the surrounding soil near the shoulder.

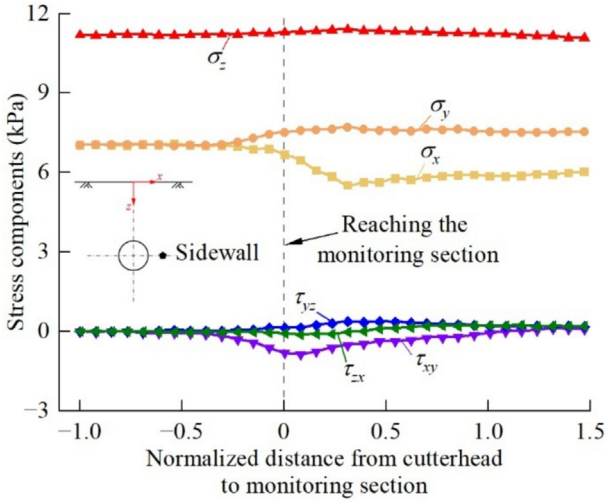

Fig. 7. Stress components of the surrounding soil near the sidewall.

release direction and principal directions of the geostatic stresses. At the monitoring point above the crown, the stress release direction is vertically downward on the transversal plane and coaxial with the vertical geostatic stress, so that τ_{zx} is equal to zero. On the other hand, the stress release direction near the shoulder points to the tunnel center, thus it is misaligned with any geostatic stresses. We can obtain τ_{zx} by decomposing the stress increment along the direction perpendicular to the major principal geostatic stress (i.e., vertical geostatic stress). This theory can also be used to explain the existence of τ_{yz} on the longitudinal plane. As for τ_{xy}, it originates from the friction between the shield machine and sand particles, so that its variation lasts for a long time.

3.3 Tunnel sidewall

Near the sidewall, σ_x decreases while σ_z hardly changes when the cutterhead passes through the monitoring section, as shown in Fig. 7. This indicates the stress release is along the horizontal direction. The decrease of σ_x vanishes after the cutterhead goes beyond the monitoring section by $0.3D$. Similar to the crown and shoulder, the sidewall sees the early response of σ_y to the arrival of the cutterhead. The difference in the final values of σ_x and σ_y demonstrates the necessity of doing a 3D analysis for the tunnel excavation problem. In addition, because the stress release direction is coaxial with the horizontal geostatic stress, τ_{zx} is almost zero. However, on the longitudinal plane and horizontal plane, both of which contain the y-axis, shear stresses cannot be ignored. Especially τ_{xy}, its variation amplitude is comparable to that of σ_y, so that the principal stress direction deviates from y-axis. τ_{xy} still evolves even when the normalized advancing distance exceeds $1.0D$, which is attributed to the continuous movement of the lining in this test. Finally, all three shear stresses turn to be zero.

3.4 Tunnel foot

The stress components near the foot are shown in Fig. 8. We can clearly observe the squeezing effect that the shield machine exerts on the surrounding soil, considering that all three normal stresses increase initially. The normalized advancing distance where σ_y begins to increase is $-0.5D$, which is also earlier than that of σ_x. The squeezing effect disappears after the cutterhead moves away. According to many numerical and analytical studies on the tunnel face stability (Huo et al., 2023; Li et al., 2023), sand that is excavated by the shield machine primarily originates from the region in front of and above the cutterhead. The shape of the loosened region looks like a funnel whose width decreases with depth. The monitoring point near the foot is not covered by the loosened region, so there is no stress release. Instead, the support pressure of the cutterhead compresses the sand and improves the normal stresses.

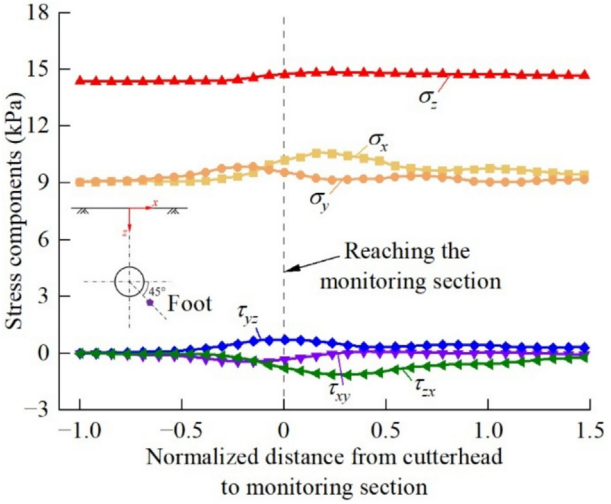

Fig. 8. Stress components of the surrounding soil near the foot.

Because the direction of the squeezing effect is misaligned with the principal directions of the geostatic stresses, shear stresses can be generated. The appearance of τ_{yz} and τ_{zx} corresponds to the same advancing distance as that of σ_y and σ_x, respectively. Only when the cutterhead approaches the monitoring section do the principal stresses on the transversal plane begin to rotate. This once again demonstrates the difference in the stress propagation speed along different directions. Among all the monitoring points, the variation amplitude of τ_{zx} near the foot is second only to that near the shoulder. In addition to this, there are many similarities between the stress states near the shoulder and foot, which will be shown later.

3.5 Tunnel invert

It can be seen from Fig. 9 that the stress components below the invert do not change much. There is a slight decrease in σ_z due to the unloading caused by tunnel excavation. In this test, the lining (i.e., polyethylene tube) is much lighter than the sand, so the influence of the self-weight of the shield machine can be ignored. The primary reason why the variation amplitude of σ_z below the invert is smaller than that above the crown is that the overlying sand partly collapses in the case of over-excavation. The only stress component whose variation amplitude can be comparable to that above the crown is τ_{yz} (note that Fig. 9 has a larger scale than Fig. 5). Notably, the signs of τ_{yz} at these two monitoring points are opposite. Overall, the influence of tunnel excavation on the stress state below the invert is very small.

4 Principal stress values

Based on six stress components in the physical space, three principal stresses can be determined by coordinate transformation. The formula is as follows:

$$\begin{bmatrix} \sigma_x & \tau_{xy} & \tau_{xz} \\ \tau_{yx} & \sigma_y & \tau_{yz} \\ \tau_{zx} & \tau_{zy} & \sigma_z \end{bmatrix} = \begin{bmatrix} \cos\alpha_1 & \cos\alpha_2 & \cos\alpha_3 \\ \cos\beta_1 & \cos\beta_2 & \cos\beta_3 \\ \cos\gamma_1 & \cos\gamma_2 & \cos\gamma_3 \end{bmatrix} \begin{bmatrix} \sigma_1 & 0 & 0 \\ 0 & \sigma_2 & 0 \\ 0 & 0 & \sigma_3 \end{bmatrix} \begin{bmatrix} \cos\alpha_1 & \cos\beta_1 & \cos\gamma_1 \\ \cos\alpha_2 & \cos\beta_2 & \cos\gamma_2 \\ \cos\alpha_3 & \cos\beta_3 & \cos\gamma_3 \end{bmatrix}, \tag{2}$$

where $\tau_{yx} = \tau_{xy}$, $\tau_{zy} = \tau_{yz}$, and $\tau_{xz} = \tau_{zx}$ according to the condition of moment equilibrium; σ_1, σ_2, and σ_3 are the major, intermediate, and minor principal stresses, respectively; α_i, β_i, and γ_i (i = 1, 2, 3) are direction angles of σ_i with respect to the x-, y- and z-axes, respectively; ($\cos\alpha_i$, $\cos\beta_i$, $\cos\gamma_i$) is the direction vector of σ_i. This section draws the stress paths in the principal stress space (σ_1, σ_2, σ_3), so that 3D stress state of the surrounding soil can be visualized intuitively.

4.1 Stress paths in 3D space

4.1.1 Tunnel crown

Figure 10 shows the 3D stress path of the surrounding soil above the crown. The starting point and the point corresponding to the arrival of cutterhead are marked to indicate the development tendency of the stress path. Besides, the 3D stress path is projected onto three 2D planes. It can be seen that at the early stage of tunnel excavation, σ_1 and σ_2 slightly increase while σ_3 decreases. When the cutterhead reaches the monitoring section, all the principal stresses rapidly decrease so that the stress path develops towards the coordinate origin. The above measured results may conflict with some FEM simulations where the transversal principal stress is found to increase after tunnel excavation (Y. Li et al., 2016; Vinoth & Aswathy, 2023). They explain that soil arching is formed above the crown,

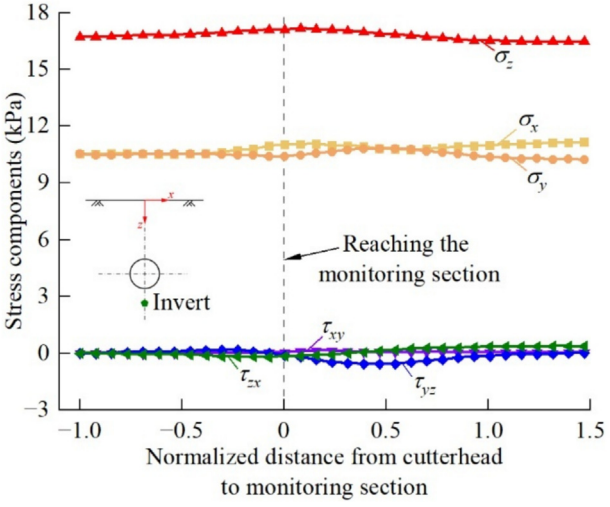

Fig. 9. Stress components of the surrounding soil below the invert.

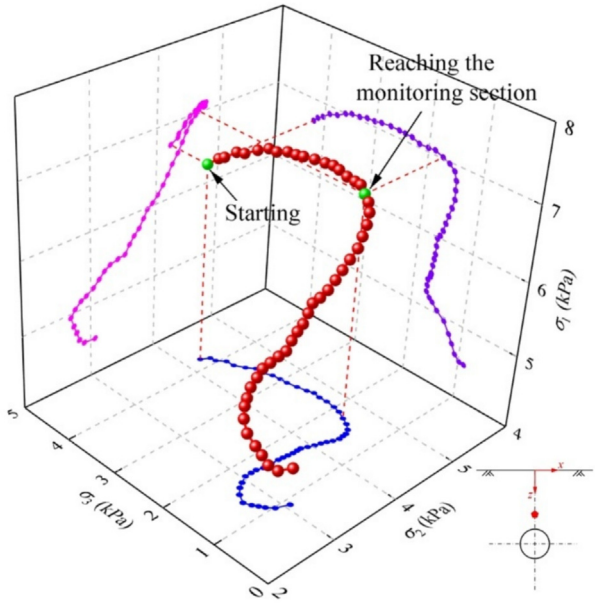

Fig. 10. Stress path of the surrounding soil above the crown in 3D space.

and the earth pressure acting on it has a horizontal component towards the tunnel centerline. In this test, the sand is very dense while the over-excavation degree is large, which brings benefits to the formation of soil arching. The position of 3D earth pressure cell is probably beyond the soil arching. Moreover, Eberhardt (2001) points out that if an elastic model is adopted to describe the stress–strain relationship of the ground, the obtained transversal principal stress will increase after tunnel excavation. But if the ground is regarded to be elastoplastic, which is the real case for geomaterials, the final values of all three principal stresses will be smaller than their initial values. This is because the soil yielding limits the increase of σ_1, and a stress redistribution exists to transfer the earth pressure in the plastic region to the region nearby. Whether the surrounding soil above the crown yields will be discussed in Section 6.2.

4.1.2 Tunnel sidewall

The 3D stress state evolution near the sidewall is the simplest among all five monitoring points. Because the shear stress components approach zero at the beginning and end of the test (see Fig. 7), we can acquire the correspondence between the normal stress components and principal stresses: σ_z is σ_1, σ_y is σ_2, and σ_x is σ_3. As shown in Fig. 11, σ_1 hardly changes before the cutterhead reaches the monitoring section. In the subsequent stage, although σ_1 experiences increasing and decreasing, its overall variation amplitude is very limited (note that the scale of the σ_1-axis is very small). The increase in σ_2 is prior to the arrival of the cutterhead, and is greater than the increase in σ_1. σ_3 keeps decreasing except it bounces back a little at last. The variation amplitude of σ_3 is the greatest, indicating the stress release is along the transversal direction. Near the sidewall, the initial stress state of the surrounding soil is triaxial compression, because $\sigma_1 > \sigma_2 = \sigma_3$ under gravity. However, tunnel excavation exerts different impacts along the transversal and longitudinal directions, so that the gap between σ_2 and σ_3 is enlarged gradually and the stress state becomes true triaxial.

4.2 Stress paths on the deviatoric plane

For simplicity, stress paths of the surrounding soil near the shoulder, foot and invert are drawn on the deviatoric plane, as shown in Fig. 12. Actually, deviatoric plane is a polar coordinate system with its polar radius being the deviatoric stress τ_π and rotation angle being the Lode's angle θ. Expressions of τ_π and θ are as follows:

$$\tau_\pi = \frac{1}{\sqrt{3}}\sqrt{(\sigma_1-\sigma_2)^2+(\sigma_2-\sigma_3)^2+(\sigma_3-\sigma_1)^2}, \tag{3}$$

$$\tan\theta = \frac{\sqrt{3}(\sigma_2-\sigma_3)}{2\sigma_1-\sigma_2-\sigma_3}, \tag{4}$$

where θ represents the relative values among the three principal stresses. Figure 12 shows that all the stress paths start from the σ_1-axis, on which $\sigma_2 = \sigma_3$ and $\theta = 0°$. For the monitoring point above the crown, both τ_π and θ increase at the beginning of tunnel excavation. However, the stress path turns around when the cutterhead reaches the monitoring section. This implies that not only the absolute values of the three principal stresses, but also their relative values, are reduced. The monitoring point is covered by the loosened region. After the cutterhead passes through the monitoring section by $0.16D$, a second turning point appears on the stress path. From then on, τ_π remains basically unchanged while θ increases to 38° until the stress state stabilizes.

Near the shoulder, the stress path continues to develop after the cutterhead passes through the monitoring section. This characteristic is different from the stress path above the crown. It indicates once again that under the current experimental conditions, the loosened region does not extend to the monitoring point near the shoulder. θ keeps

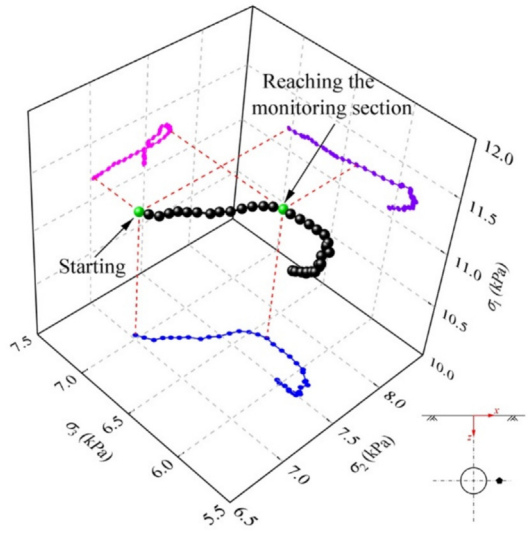

Fig. 11. Stress path of the surrounding soil near the sidewall in 3D space.

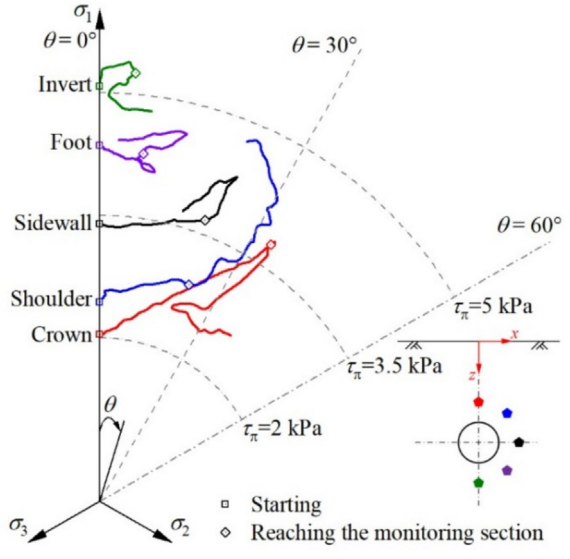

Fig. 12. Stress paths of the surrounding soil on the deviatoric plane.

to be 30° for a long time, so that σ_2 is equal to $(\sigma_1 + \sigma_3)/2$. In the end, the value of τ_π is larger than that above the crown. Note that the normal stress corresponding to the deviatoric plane $\sigma_\pi = \frac{1}{\sqrt{3}}(\sigma_1 + \sigma_2 + \sigma_3)$ near the shoulder can be relatively larger, due to the deeper burial position of the 3D earth pressure cell and lower degree of stress release. Therefore, the surrounding soil here has a higher shear strength.

Near the sidewall, τ_π gradually increases, especially when the cutterhead passes through the monitoring section. Considering the limited variation amplitude of σ_1, we can deduce that the increase in τ_π results from the decrease in σ_3 and the enlarging gap between σ_2 and σ_3. After the normalized advancing distance exceeds $0.3D$, the stress path turns around due to the recovery of σ_3. This turning point can also be observed from Fig. 11.

Interestingly, the three-staged variation rule of τ_π and θ below the invert is very similar to that above the crown, except that the former variation amplitude is relatively smaller. Stress paths near the foot and shoulder also have many similarities in terms of their development tendency. This is attributed to the symmetry of the monitoring points about the tunnel springline (Barla, 2008). In general, as the burial depth decreases, the stress path gets longer and the Lode's angle becomes greater after tunnel excavation, so that the corresponding stress state deviates more from triaxial compression.

5 Principal stress directions

According to Eq. (2), direction angles of the principal stresses with respect to the coordinate axes in the physical space can be calculated together with the principal stress values. This section analyzes the variation of these angles to investigate the principal stress rotation during tunnel excavation.

5.1 Direction angles of the principal stresses

There are nine direction angles in total for three principal stresses with respect to three coordinate axes, but only three of them are independent. Here, γ_1 (angle between σ_1 and z-axis), β_2 (angle between σ_2 and y-axis), and α_3 (angle between σ_3 and x-axis) are chosen. In Fig. 13(a), the major principal stress direction is illustrated by a small vector at the data point, and the angle between this vector and the vertical direction of the figure is equal to γ_1. In Fig. 13(b) and (c), the vector inclines by an angle of β_2 or α_3 from the horizontal direction. The vertical coordinate of Fig. 13 denotes the principal stress value, which has been introduced in Section 4. It can be seen from Fig. 13(a) that σ_1 is along the z-axis (i.e., $\gamma_1 = 0°$) at the beginning of tunnel excavation, because the vertical geostatic stress is larger than the horizontal geostatic stress ($K_0 < 1$). For the surrounding soil above the crown, the direction of σ_1 quickly rotates when the cutterhead passes through the monitoring section. Accompanied by the convergence of its value, the rotation of σ_1 also stops. Finally, γ_1 is equal to about 30°. The rotation of σ_2 appears much earlier, as β_2 has already reduced to 70° at the moment of passage. In the end, α_3 is less than 15°, indicating that σ_3 is relatively biased towards the x-axis. This conclusion can also be obtained from Fig. 5, which shows that σ_x is smaller than the other two normal stress components.

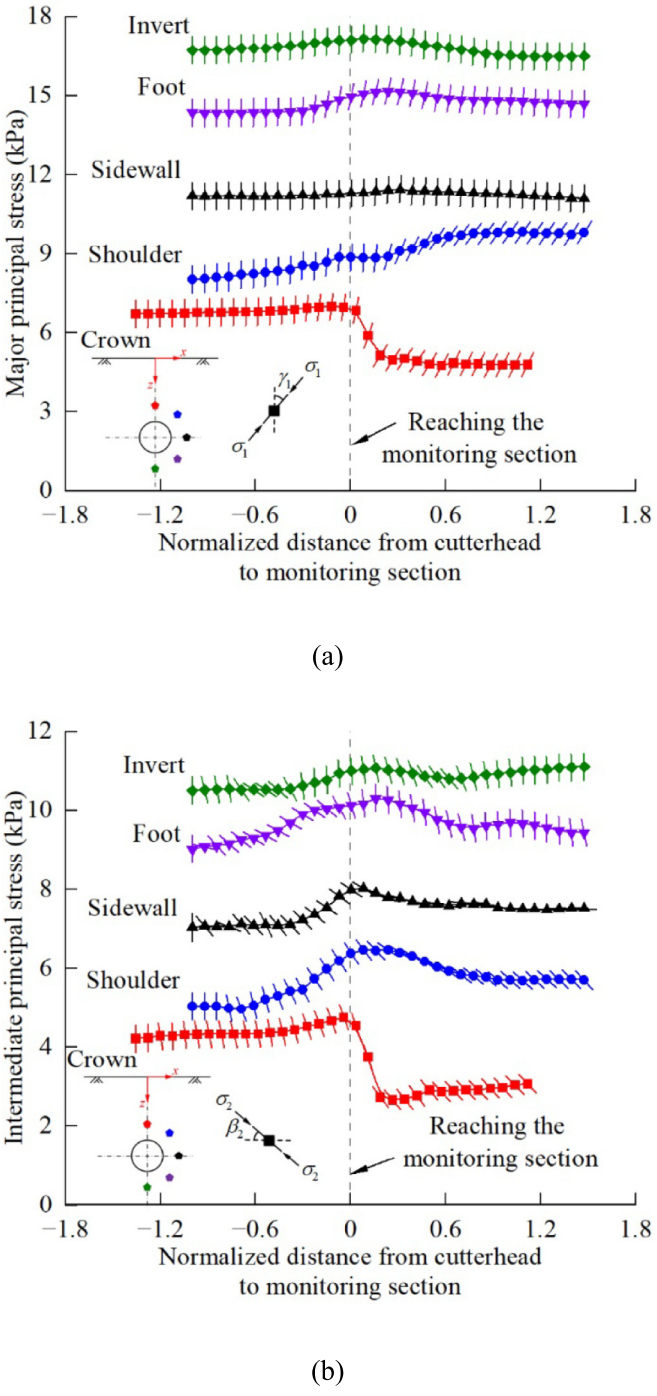

Fig. 13. Principal stress directions of the surrounding soil. (a) Direction angle of σ_1 with respect to z-axis, (b) direction angle of σ_2 with respect to y-axis, and (c) direction angle of σ_3 with respect to x-axis.

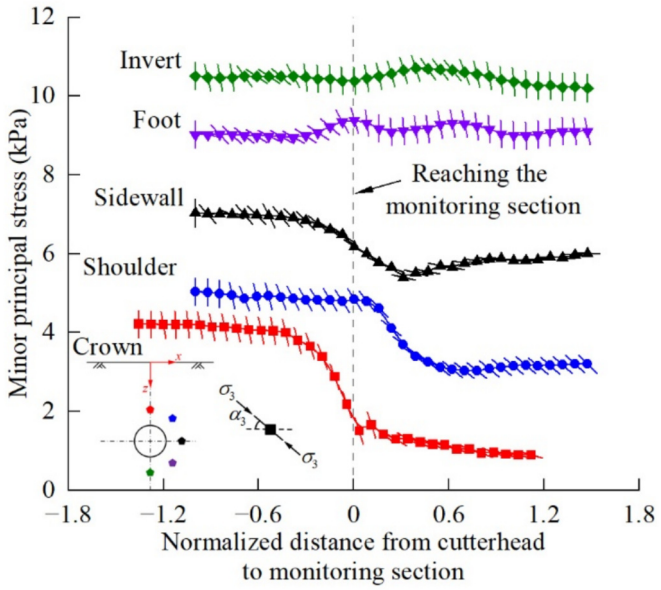

(c)

Fig 13. *(continued)*

Near the shoulder, the maximum angle between σ_1 and z-axis is up to 40°, which appears during shield undercrossing and is larger than γ_1 above the crown. Moreover, σ_2 and σ_3 start rotating when the monitoring section is $0.8D$ ahead of the cutterhead. Their rotation angles become the greatest when the monitoring section is reached, i.e., $\beta_2 = 29°$ and $\alpha_3 = 34°$. Then, σ_2 and σ_3 rotate back to some extent, but none of the principal stresses are parallel to the coordinate axis of the physical space. Note that the principal stress rotation near the shoulder has been found in many FEM simulations (Fang et al., 2022; Ng et al., 2013), while our work confirms its existence by laboratory test. The measured results further show that in the 3D space, the principal stress rotation is quite complicated, because the starting time, variation rule, and ending time of the three principal stresses are different.

Near the sidewall, the direction of σ_1 keeps vertical (i.e., $\gamma_1 = 0°$) during the whole excavation process. Principal stress rotation only occurs on the horizontal plane, so that the variation rule of β_2 and α_3 is consistent. There is an obvious fluctuation in β_2 and α_3 at the beginning, because σ_x and σ_y are almost equal, and a subtle disturbance in their values will lead to an abrupt exchange of the directions of σ_2 and σ_3. In the end, σ_2 is parallel to the shield advancing direction while σ_3 is along the transversal direction.

Near the foot, all the principal stresses rotate when the cutterhead approaches and passes through the monitoring section. However, their directions gradually return to the initial state as the cutterhead moves away. This indicates that the squeezing effect caused by shield advancing (mentioned in Section 3.4) cannot change the stress state of the surrounding soil permanently. A similar development tendency was observed in the model test of Li et al. (2024).

Below the invert, the rotation of the three principal stresses is not very obvious, due to the limited stress release amplitude. Principal stress rotation appears only when σ_x and σ_y are close to each other, which belongs to a mathematical problem but has no physical meaning.

5.2 Principal stress rotation on the longitudinal plane

From this section, a special coordinate system is introduced to display the principal stress rotation more clearly. In Fig. 14, the horizontal coordinate axis is $(\sigma_y–\sigma_z)/2$ while the vertical coordinate axis is τ_{yz}. For a stress state point in this coordinate system, its connecting line with the coordinate origin has the following characteristics according to the knowledge of Mohr's circle. The length of this connecting line is equal to

$$\sqrt{\left(\frac{\sigma_y-\sigma_z}{2}\right)^2+\tau_{yz}^2}=\frac{\sigma_1^{\mathrm{l}}-\sigma_3^{\mathrm{l}}}{2}, \tag{5}$$

where σ_1^{l} and σ_3^{l} are the major and minor principal stresses on the longitudinal plane, respectively; superscript l is added to distinguish them from the principal stresses in 3D space. Besides, the rotation angle from the positive part of the horizontal coordinate axis to the connecting line is equal to

$$\tan^{-1}\frac{2\tau_{yz}}{\sigma_y-\sigma_z}=2\alpha^{\mathrm{l}}, \tag{6}$$

where α^{l} is the direction angle of σ_1^{l} with respect to the y-axis in practice. Therefore, from this coordinate system, we can observe the principal stress rotation on the longitudinal plane.

As a representative, the stress state above the crown is drawn in Fig. 14. The starting point is located on the negative part of the horizontal coordinate axis, which means $\alpha^{\mathrm{l}} = 90°$ and σ_1^{l} is along the z-axis. With the shield machine advancing, sand in front of and above the cutterhead is excavated, so that a loosened region is formed. The stress

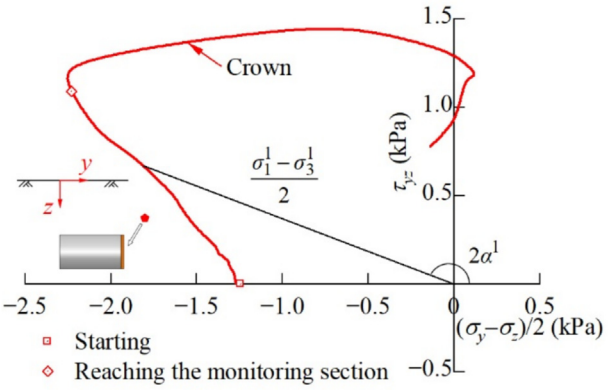

Fig. 14. Principal stress rotation of the surrounding soil above the crown on the longitudinal plane.

release direction points to the cutterhead, causing a stress increment that is misaligned with the vertical or horizontal geostatic stress. Therefore, if the vector sum of the geostatic stress and stress increment is calculated to determine the current stress state, shear stress will be generated, and the direction of σ_1^l gradually deviates from z-axis. When the cutterhead is just beneath the monitoring point, the stress release direction becomes coaxial with the vertical geostatic stress. No shear stress is generated at this moment, so that τ_{yz} and $\left(\sigma_1^l - \sigma_3^l\right)/2$ (which is equal to the maximum shear stress on the longitudinal plane) reach the peak. Then, α^l continues to increase with the variation of normal stresses. The stress state point can arrive at the first quadrant of the coordinate system, indicating that the direction of σ_1^l is closer to y-axis.

5.3 Principal stress rotation on the transversal plane

Figure 15 shows the stress states near the shoulder and foot in the coordinate system of $(\sigma_z–\sigma_x)/2$-τ_{zx}, to analyze the principal stress rotation on the transversal plane. We can find that the stress paths at these two monitoring points have opposite development tendencies. This is because stress release occurs in the surrounding soil near the shoulder, while the squeezing effect is dominating near the foot, as has been pointed out in Section 3. The principal stress direction near the shoulder begins to rotate remarkably after the cutterhead has already passed through the monitoring section. This phenomenon indicates that the surrounding soil makes a delayed response to the stress release on the transversal plane, and the stress propagation along the transversal direction is lagging behind the longitudinal direction. The maximum rotation angle of the major principal stress on the transversal plane from z-axis, i.e., α^t, is up to 31° near the shoulder and –14° near the foot. When the cutterhead moves far away, α^t near the foot reduces to –3°, so that the principal stress rotation here is recoverable.

5.4 Principal stress rotation on the horizontal plane

On the horizontal plane, the stress state at the sidewall is illustrated in the coordinate system of $(\sigma_x–\sigma_y)/2$-τ_{xy}, as shown in Fig. 16. Because $\sigma_x = \sigma_y$ and $\tau_{xy} = 0$ at the beginning, we cannot identify the major principal stress direction on the horizontal plane. With the shield machine advancing, the stress release direction always points to the cutterhead so that it is misaligned with either x-axis or y-axis. As a result, τ_{xy} appears, and the principal stress direction rotates. More importantly, τ_{xy} can be produced by the friction between the shield machine and sand particles. Note that in our shield machine, the diameter of the cutterhead is slightly larger than that of the lining, facilitating the movement of the lining together with the cutterhead. The friction becomes the most intense when the cutterhead reaches the monitoring section. After that, τ_{xy} reduces to zero, and the major principal stress direction on the horizontal plane is along the y-axis.

6 Discussion

6.1 Influence of K_0-value

In the above sections, the stress state of the surrounding soil is determined by adding the geostatic stress, which is calculated by theoretical formulas, and the stress increment, which is measured by the 3D earth pressure cell. This treatment is adopted because it is hard to accurately measure the initial stress state of the ground. According to the parametric study in some numerical simulations (Eberhardt, 2001; Zhao et al., 2023), the value of K_0 will influence the stress field after tunnel excavation. Figure 17 shows the stress paths above the crown on the meridian plane under different values of K_0. As the shield machine advances, the mean stress p $(= \sigma_\pi/\sqrt{3})$ monotonically

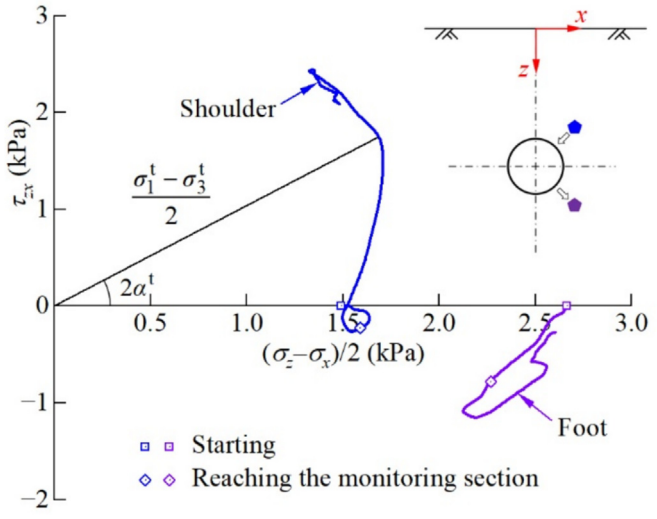

Fig. 15. Principal stress rotation of the surrounding soil near the shoulder and foot on the transversal plane.

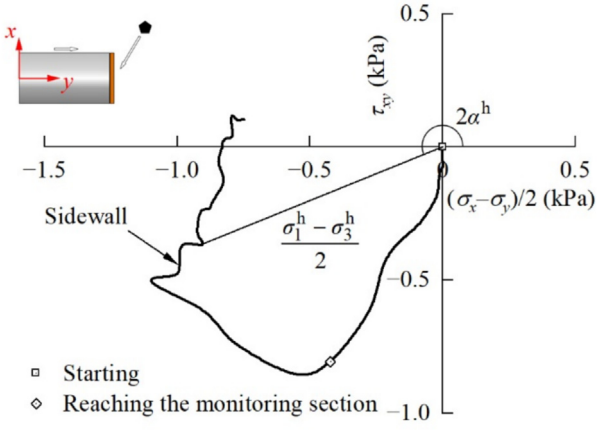

Fig. 16. Principal stress rotation of the surrounding soil near the sidewall on the horizontal plane.

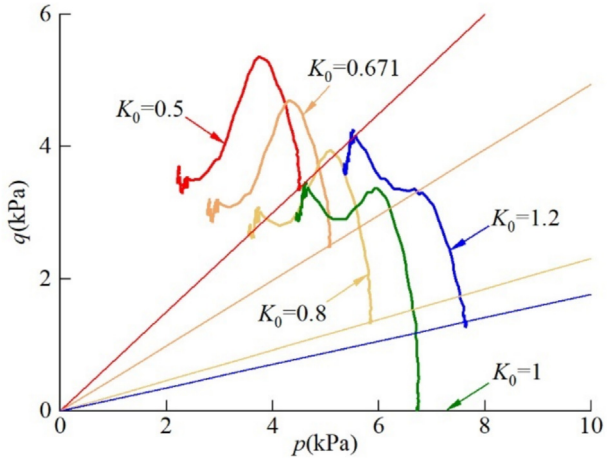

Fig. 17. Influence of K_0-value on the stress path above the crown.

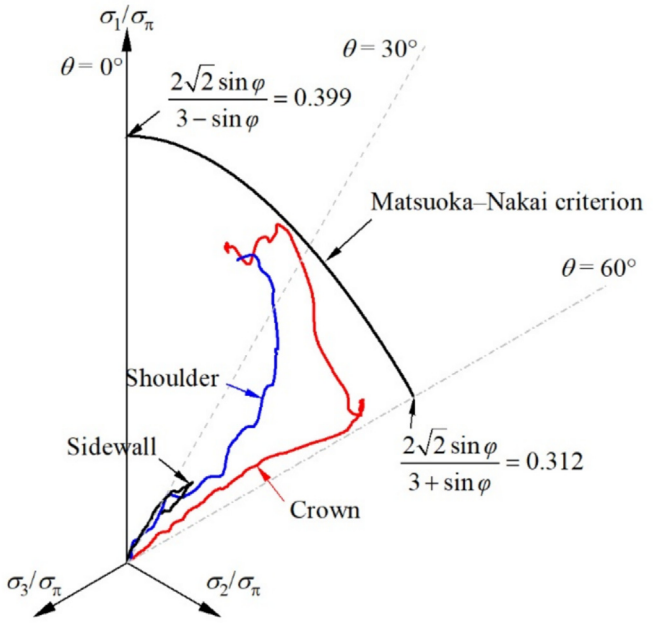

Fig. 18. Stress paths of the surrounding soil on the normalized deviatoric plane.

decreases, while the deviatoric stress q ($= \sqrt{3/2}\tau_\pi$) first increases and then decreases. K_0-value can alter the starting point of the stress path and the variation amplitude of q, but it cannot influence the development tendency of the stress path. When $K_0 > 1$, σ_z becomes the minor principal stress at the beginning of tunnel excavation, so that the principal stress direction is different from the case of $K_0 < 1$. However, in the coordinate systems of Figs. 14–16, the stress path only moves left or right without a shape change under different K_0-values, which means the rotation rule of the principal stress is identical.

6.2 Failure of the surrounding soil

To analyze the failure of the surrounding soil, stress paths are redrawn on the normalized deviatoric plane, as shown in Fig. 18. Each stress state is normalized by its corresponding σ_π, so that the stress ratio τ_π/σ_π can be recognized. The frictional property of soil is grasped via this normalization. On the other hand, failure envelope is determined by Matsuoka–Nakai criterion

$$\frac{(\sigma_1+\sigma_2+\sigma_3)(\sigma_1\sigma_2+\sigma_2\sigma_3+\sigma_3\sigma_1)}{\sigma_1\sigma_2\sigma_3} = 8\tan^2\varphi + 9, \qquad (7)$$

where $\varphi = 21.9°$. Note that on the normalized deviatoric plane, the failure envelope of the Matsuoka–Nakai criterion is unique for different values of σ_π. From the stress path above the crown, we can find that τ_π/σ_π gradually increases until the stress state point approaches the failure envelope. This indicates that the surrounding soil above the crown fails. The failure stress state corresponds to a Lode's angle of 26°, so that Matsuoka–Nakai criterion, rather than Mohr–Coulomb criterion, is adopted to consider the effect of the intermediate principal stress. In some numerical simulations (Miliziano & De Lillis, 2019; Zheng et al., 2015), σ_3 above the crown reduces to zero, which means the soil failure is caused by tensile stress. In this test, the surrounding soil does not collapse completely because it is compacted to be very dense, but failure still occurs under the action of shear stress. σ_3 converges to a small positive value, and the tunneling-induced stress release will be undertaken by the soil nearby. On the normalized deviatoric plane, the stress path near the shoulder is shorter than that above the crown, due to a larger σ_π. As for the other monitoring points, the stress paths are far from the failure envelope, so that the surrounding soil does not fail.

6.3 Comparison of the measured results with numerical simulations

When the measured results are introduced in the above sections, we have compared them with some numerical simulations. Overall, the measured and simulated results are basically consistent in terms of the qualitative rule. However, the existing numerical simulations cannot reproduce the stress characteristics of the surrounding soil in some aspects. We certainly cannot completely trust the measured results, because errors can be caused by many factors, such as the precision of the 3D earth pressure cell, disturbance from the soil filling and compacting process, displacement and inclination of the 3D earth pressure cell during tunnel excavation, and so on. Deviations between the measured and simulated results mainly exist in the following aspects. According to the measured results, sensors perceive the stress variation only when the cutterhead is quite close to the monitoring section (see Figs. 5–9). This is attributed to the fact that soil is a kind of discrete medium in which the energy dissipation is severe. However, in many FEM simulations, including those done by ourselves, the stress variation always appears early and converges late. Besides, the numerical simulations cannot distinguish the stress propagation speed along different directions, while the

measured value of σ_y varies before σ_x and σ_z begin to evolve. The rotation of σ_1 (which is relatively closer to the vertical direction) also lags behind that of σ_2 and σ_3 (see Fig. 13).

In order to improve the numerical simulation results, we should introduce an advanced constitutive model for soil. As the tunneling-induced stress redistribution is very complicated, the stress path dependence, the effects of intermediate principal stress and principal stress rotation, as well as the soil anisotropy, should be considered. A proper yield surface and corresponding loading–unloading criterion should also be adopted in the constitutive model. Because the stress path above the crown develops towards upper left on the meridian plane (see Fig. 17), which is different from the conventional loading conditions, the elliptical yield surface of the modified Cam-clay model or the capped yield surface of the Drucker–Prager model will regard the stress–strain relationship to be elastic. Consequently, the soil deformation during tunnel excavation will be underestimated. In addition, the strategy for simulating the tunnel excavation process is also very important. The over-excavation degree, advancing and rotation of the cutterhead, and friction between the shield machine and soil can influence the stress value more or less. Because stress leads to strain, a better understanding of the 3D stress state of the surrounding soil helps to calculate the ground deformation induced by tunnel excavation accurately.

7 Conclusions

This paper adopts a scaled shield machine to simulate the tunnel excavation process in the laboratory. The stress state of the surrounding soil is measured by a 3D earth pressure cell. Based on the test data, we can find the following characteristics of the tunneling-induced ground stresses.

(1) In terms of the stress values, the normal stress components and principal stresses above the crown decrease, but the longitudinal normal stress σ_y can recover as the cutterhead moves away. The stress state at failure satisfies Matsuoka–Nakai criterion. The normal stress variation near the shoulder is relatively small, but the shear stress components and deviatoric stress are considerable. The stress release near the sidewall is along the horizontal direction on the transversal plane, leading to a true triaxial stress state after tunnel excavation. Due to the squeezing effect, all three normal stresses near the foot increase before the cutterhead reaches the monitoring section. On the deviatoric plane, stress paths near the foot and invert are similar to those near the shoulder and crown, respectively, except that the stress path gets longer at shallower monitoring points.

(2) When the stress release direction is misaligned with any principal directions of the geostatic stresses, shear stress will be generated in the physical space, and thus the principal stress axes rotate. Above the crown, the major principal stress σ_1 is vertical at the beginning, but rotates quickly towards the longitudinal direction when the cutterhead passes through the monitoring section. On the transversal plane, the principal stresses near the shoulder and foot have opposite rotation directions, because stress release occurs in the former while the squeezing effect is dominating in the latter. Besides, the stress propagation speed along the longitudinal direction is generally faster than that along the transversal direction.

Limited by the size of the laboratory test, this work only measures the stress state of the surrounding soil at several representative points around the tunnel. The stress redistribution at different distances from the tunnel center cannot be analyzed. The measured results can be adopted to calibrate the material parameters and modeling strategies in the numerical simulations, so that the stress field of the whole ground, as well as the loosened region and soil arching effect, can be obtained in the future.

Data availability

The data that support the findings of this study are available from the corresponding author upon reasonable request.

CRediT authorship contribution statement

Yu Tian: Methodology, Data curation, Writing – original draft, Formal analysis, Conceptualization. **Hao Chen:** Writing – original draft, Visualization, Formal analysis, Methodology. **Junquan Wen:** Writing – original draft, Formal analysis, Methodology. **Abdul Motalleb Qaytmas:** Methodology, Writing – original draft, Data curation. **Dechun Lu:** Writing – review & editing, Funding acquisition, Supervision. **Xiuli Du:** Supervision, Funding acquisition, Writing – review & editing.

Declaration of competing interest

The authors declare that they have no known competing financial interests or personal relationships that could have appeared to influence the work reported in this paper.

Acknowledgement

This work was supported by the National Key R&D Program of China (Grant No. 2022YFC3800901) and the National Natural Science Foundation of China (Grant No. 51908010).

References

Ahmed, A., Islam, M. A., Alam, M. Z., & Quazi, H. S. (2023). Surface settlement induced by horizontal directional drilling. *Underground Space, 8*, 94–108.

Barla, M. (2008). Numerical simulation of the swelling behaviour around tunnels based on special triaxial tests. *Tunnelling and Underground Space Technology, 23*(5), 508–521.

Berthoz, N., Branque, D., Wong, H., & Subrin, D. (2018). TBM soft ground interaction: Experimental study on a 1 g reduced-scale EPBS model. *Tunnelling and Underground Space Technology, 72*, 189–209.

Eberhardt, E. (2001). Numerical modelling of three-dimension stress rotation ahead of an advancing tunnel face. *International Journal of Rock Mechanics and Mining Sciences, 38*(4), 499–518.

Fang, Y., Cui, J., Wanatowski, D., Nikitas, N., Yuan, R., & He, Y. (2022). Subsurface settlements of shield tunneling predicted by 2D and 3D constitutive models considering non-coaxiality and soil anisotropy: A case study. *Canadian Geotechnical Journal, 59*(3), 424–440.

Feng, X. T., Xu, H., Yang, C. X., Zhang, X. W., & Gao, Y. H. (2020). Influence of loading and unloading stress paths on the deformation and failure features of Jinping marble under true triaxial compression. *Rock Mechanics and Rock Engineering, 53*(7), 3287–3301.

Gu, L. J., Feng, X. T., Kong, R., Yang, C. X., Han, Q., & Xia, Y. L. (2023). Excavation stress path induced fracturing mechanism of hard rock in deep tunnel. *Rock Mechanics and Rock Engineering, 56*(3), 1779–1806.

Huang, F., Shi, X. X., Wu, C. Z., Dong, G. F., Liu, X. C., & Zheng, A. C. (2023). Stability analysis of tunnel under coal seam goaf: Numerical and physical modeling. *Underground Space, 11*, 246–261.

Huo, M. Z., Chen, W. Z., Wu, G. J., Yuan, J. Q., & Li, Y. F. (2023). Probabilistic analysis of tunnel face stability in spatially variable soil. *Tunnelling and Underground Space Technology, 141*, 105327.

Jiang, M. J., Sima, J., Cui, Y. J., Hu, H. J., Zhou, C. B., & Lei, H. Y. (2017). Experimental investigation of the deformation characteristics of natural loess under the stress paths in shield tunnel excavation. *International Journal of Geomechanics, 17*(9), 04017079.

Jiang, M. J., & Yin, Z. Y. (2012). Analysis of stress redistribution in soil and earth pressure on tunnel lining using the discrete element method. *Tunnelling and Underground Space Technology, 32*, 251–259.

Lee, K. M., & Rowe, R. K. (1989). Deformations caused by surface loading and tunnelling: The role of elastic anisotropy. *Géotechnique, 39*(1), 125–140.

Li, W., Zhang, C. P., Tu, S. Q., Chen, W., & Ma, M. S. (2023). Face stability analysis of a shield tunnel excavated along inclined strata. *Underground Space, 13*, 183–204.

Li, X. B., Cao, W. Z., Tao, M., Zhou, Z. L., & Chen, Z. H. (2016a). Influence of unloading disturbance on adjacent tunnels. *International Journal of Rock Mechanics and Mining Sciences, 84*, 10–24.

Li, Y., Wang, R., Ma, H. B., & Zhang, J. M. (2025). Rising groundwater table due to restoration projects amplifies earthquake induced liquefaction risk in Beijing. *Nature Communications, 16*(1), 1466.

Li, Y. F., Wu, G. J., Chen, W. Z., Yuan, J. Q., Huo, M. Z., & Liu, Y. B. (2024). Laboratory experimental study of the forming and failure mechanisms of soil arching during EPBS tunnelling in sand. *Engineering Failure Analysis, 163*, 108518.

Li, Y. Y., Jin, X. G., Lyu, Z. T., Dong, J. H., & Guo, J. C. (2016b). Deformation and mechanical characteristics of tunnel lining in tunnel intersection between subway station tunnel and construction tunnel. *Tunnelling and Underground Space Technology, 56*, 22–33.

Lin, X. T., Chen, R. P., Wu, H. N., & Cheng, H. Z. (2019). Three-dimensional stress-transfer mechanism and soil arching evolution induced by shield tunneling in sandy ground. *Tunnelling and Underground Space Technology, 93*, 103104.

Lyu, X. L., Zeng, S., Zhao, Y. C., Huang, M. S., Ma, S. K., & Zhang, Z. G. (2020). Physical model tests and discrete element simulation of shield tunnel face stability in anisotropic granular media. *Acta Geotechnica, 15*(10), 3017–3026.

Mašín, D. (2009). 3D modeling of an NATM tunnel in high K_0 clay using two different constitutive models. *Journal of Geotechnical and Geoenvironmental Engineering, 135*(9), 1326–1335.

Massinas, S. A., & Sakellariou, M. G. (2009). Closed-form solution for plastic zone formation around a circular tunnel in half-space obeying Mohr–Coulomb criterion. *Géotechnique, 59*(8), 691–701.

Miliziano, S., & De Lillis, A. (2019). Predicted and observed settlements induced by the mechanized tunnel excavation of metro line C near S. Giovanni station in Rome. *Tunnelling and Underground Space Technology, 86*, 236–246.

Ng, C. W. W., Boonyarak, T., & Mašín, D. (2013). Three-dimensional centrifuge and numerical modeling of the interaction between perpendicularly crossing tunnels. *Canadian Geotechnical Journal, 50*(9), 935–946.

Ng, C. W. W., Wong, A. Y. Y., Buenaventura, A. D. F., & Zhu, P. Y. (2024). Three-dimensional numerical analysis of twin tunnelling in two-layered soil strata. *Tunnelling and Underground Space Technology, 153*, 106028.

Tian, Y., Qaytmas, A. M., Lu, D. C., & Du, X. L. (2023). Stress path of the surrounding soil during tunnel excavation: An experimental study. *Transportation Geotechnics, 38*, 100917.

Vinoth, M., & Aswathy, M. S. (2023). 3D Evolution of soil arching during shield tunnelling in silty and sandy soils: A comparative study. *International Journal for Numerical and Analytical Methods in Geomechanics, 47*(2), 299–322.

Wang, H. N., Wu, L., & Jiang, M. J. (2020). Viscoelastic ground responses around shallow tunnels considering surcharge loadings and effect of supporting. *European Journal of Environmental and Civil Engineering, 24*(13), 2306–2328.

Wang, Y. Q., Liu, Y., Wang, Z. F., Zhang, X., Hui, Y. C., & Li, J. C. (2023). Investigation on progressive failure process of tunnel lining induced by creep effect of surrounding rock: A case study. *Engineering Failure Analysis, 144*, 106946.

Wang, Z. C., Wong, R. C. K., Li, S. C., & Qiao, L. P. (2012). Finite element analysis of long-term surface settlement above a shallow tunnel in soft ground. *Tunnelling and Underground Space Technology, 30*, 85–92.

Yuan, R., Qiu, Y., & Cheng, Y. (2024). A framework of probabilistic seismic risk analysis of urban shallow-buried tunnels subjected to active fault dislocations. *Journal of Earthquake Engineering, 28*(5), 1312–1330.

Zhang, P., Du, X. L., Lu, D. C., Jin, L., & Qi, J. L. (2021a). Study on the excavation disturbed zone during tunneling in sandy cobble stratum considering the material meso-structure. *Transportation Geotechnics, 29*, 100590.

Zhang, P., Lu, D. C., Du, X. L., & Qi, J. L. (2021b). A division method for shallow tunnels and deep tunnels considering soil stress path dependency. *Computers and Geotechnics, 135*, 104012.

Zhao, R., Tao, M., Zhao, H. T., Wu, C. Q., & Cao, W. Z. (2023). Theoretical study on dynamic stress redistribution around circular tunnel with different unloading paths. *Computers and Geotechnics, 163*, 105737.

Zheng, G., Lu, P., & Diao, Y. (2015). Advance speed-based parametric study of greenfield deformation induced by EPBM tunneling in soft ground. *Computers and Geotechnics, 65*, 220–232.